J Biol Inorg Chem (2005) 10: 51–62
DOI 10.1007/s00775-004-0613-5

ORIGINAL ARTICLE

Stefanie Foerster · Maurice van Gastel · Marc Brecht
Wolfgang Lubitz

# An orientation-selected ENDOR and HYSCORE study of the Ni-C active state of *Desulfovibrio vulgaris* Miyazaki F hydrogenase

Received: 16 September 2004 / Accepted: 9 November 2004 / Published online: 21 December 2004


**Abstract** Electron nuclear double resonance (ENDOR) and hyperfine sublevel correlation spectroscopy (HYSCORE) are applied to study the active site of catalytic [NiFe]-hydrogenase from *Desulfovibrio vulgaris* Miyazaki F in the reduced Ni-C state. These techniques offer a powerful tool for detecting nearby magnetic nuclei, including a metal-bound substrate hydrogen, and for mapping the spin density distribution of the unpaired electron at the active site. The observed hyperfine couplings are assigned via comparison with structural data from X-ray crystallography and knowledge of the complete *g*-tensor in the Ni-C state (Foerster et al. (2003) J Am Chem Soc 125:83–93). This is found to be in good agreement with density functional theory calculations. The two most strongly coupled protons ($a_{iso} = 13.7$, 11.8 MHz) are assigned to the $\beta$-$CH_2$ protons of the nickel-coordinating cysteine 549, and a third proton ($a_{iso} = 8.9$ MHz) is assigned to a $\beta$-$CH_2$ proton of cysteine 546. Using $D_2O$ exchange experiments, the presence of a hydride in the bridging position between the nickel and iron—recently been detected for a regulatory hydrogenase (Brecht et al. (2003) J Am Chem Soc 125:13075–13083)—is experimentally confirmed for the first time for catalytic hydrogenases. The hydride exhibits a small isotropic hyperfine coupling constant ($a_{iso} = -3.5$ MHz) since it is bound to Ni in a direction perpendicular to the *z*-axis of the Ni ($3d_{z^2}$) orbital. Nitrogen signals that belong to the nitrogen $N_\epsilon$ of His-88 have been identified. This residue forms a hydrogen bond with the spin-carrying Ni-coordinated sulfur of Cys-549. Comparison with other hydrogenases reveals that the active site is essentially the same in all proteins, including a regulatory hydrogenase.

**Keywords** Hydrogenase · ENDOR · HYSCORE · Nickel enzymes

S. Foerster · M. van Gastel · W. Lubitz (✉)
Max-Planck-Institut für Bioanorganische Chemie,
P.O. Box 10 13 65, 45413 Mülheim an der Ruhr, Germany
E-mail: lubitz@mpi-muelheim.mpg.de
Tel.: +49-208-306-3614
Fax: +49-208-306-3955

S. Foerster · M. Brecht
Max-Volmer-Laboratorium für Biophysikalische Chemie,
Fakultät für Mathematik und Naturwissenschaften,
Technische Universität Berlin, 10623 Berlin, Germany

*Present address*: M. Brecht
Institut für Experimentalphysik, Freie Universität Berlin,
Arnimallee 14, 14195 Berlin, Germany

## Introduction

Hydrogenases comprise a fundamental group of bacterial enzymes that catalyze the reversible oxidation of molecular hydrogen to protons, and play a vital role in the anaerobic metabolisms of a wide variety of microorganisms [1, 2]. Three phylogenetically distinct classes of hydrogenases have been discovered so far, that differ in terms of their metal content [3]. Among those, [NiFe]-hydrogenases represent the largest class. Many organisms contain two or more different [NiFe]-hydrogenases situated in different cell compartments. Their function (hydrogen uptake or production) is associated with their respective locations in the cell. The diversity of the hydrogenases in these bacteria demonstrates the important role of hydrogen in their metabolism. Moreover, regulatory [NiFe]-hydrogenases are also present, which ensure a rapid and efficient response to variations in energetic needs under changing growth conditions.

During catalysis, hydrogenase cycles through various redox states, several of which are paramagnetic. The oxidized enzyme displays two different EPR signals, termed Ni-A (“unready”) and Ni-B (“ready”) [4, 5]. Under reductive conditions another characteristic EPR signal appears, named Ni-C (“active”). This signal is associated with the catalytically active state since it is also observed during hydrogenase catalysis in vivo [6]. The reduced form of hydrogenase is capable to catalyze proton–deuterium or proton–tritium exchange in the

absence of electron donors or acceptors, according to the reaction $H_2 + D_2O \rightarrow HD + HDO$. This finding indicates the direct accessibility of the active site in the Ni-C state to molecular hydrogen. Furthermore, it suggests that molecular hydrogen is heterolytically cleaved, producing a proton and a hydride and the subsequent formation of an enzyme-hydride intermediate [7–9].

The [NiFe]-hydrogenase of *D. vulgaris* Miyazaki F consists of a large and a small subunit. The crystal structure of the enzyme has been solved to 1.8 Å resolution [10]. Three [FeS] clusters are present in the small subunit and the active site is buried deeply in the large subunit. The active site is depicted schematically in Fig. 1 and consists of iron and nickel that are bridged by two cysteines. The nickel is further ligated by two terminal cysteines and the iron has three diatomic inorganic ligands. Although the conformation of the active site is found to be conserved for many [NiFe]-hydrogenases [10–14], disagreement between the crystal structures exists with respect to the nature of the diatomic ligands to iron. In *D. vulgaris* Miyazaki F they are assigned to one SO and two CN ligands [10], whereas in all other crystal structures one CO and two CNs are found [11–14]. Recent infrared absorption measurements have, however, unequivocally established that the [NiFe]-hydrogenase of *D. vulgaris* Miyazaki F also has one CO and two $CN^-$ ligands (C. Fichtner et al., Max-Planck-Institut für Bioanorganische Chemie, unpublished data, 2004).

In the crystal structures of the as-isolated, oxidized states Ni-A and Ni-B, additional electron density is found between Ni and Fe, which stems from a third bridging ligand. This ligand is most likely an oxygen ligand [11, 15–17]. In the active state, called Ni-C, which is two electrons more reduced than Ni-A and Ni-B, this electron density is absent [18, 19]. A large $^1H$ hyperfine interaction has been found in electron nuclear double resonance (ENDOR) experiments [20, 21], from which a hydride bridge for the reduced state was postulated. Recently, the complete hyperfine tensor of the hydride bridge was determined from hyperfine sublevel correlation (HYSCORE) spectroscopy of the regulatory hydrogenase of *Ralstonia eutropha* in the Ni-C state [22].

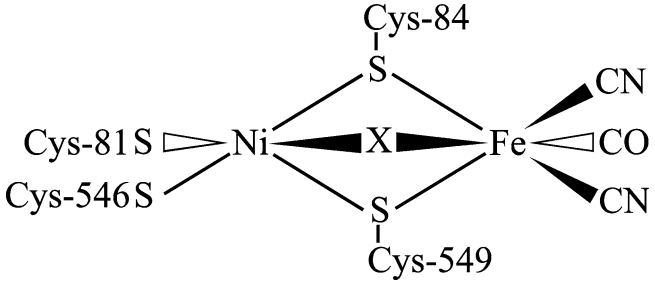


**Fig. 1** Schematic representation of the active site of the [NiFe]-hydrogenase of *D. vulgaris* Miyazaki F. The bridging ligand "*X*" is suggested to be an oxygenic species in the oxidized state [11, 16, 17] and a hydride in the reduced state [20–23]

In order to understand the reaction mechanism of the [NiFe]-hydrogenase, details about the electronic structure of the active site are required. Recently, we determined the orientation of the *g*-tensor of the Ni-C state for *D. vulgaris* Miyazaki F hydrogenase by single crystal EPR spectroscopy [23]. The principal axis that corresponds to the smallest *g* value ($g_z$ or $g_3$) was found to lie almost parallel to the bond direction of Ni and the sulfur of Cys-549 (one of the bridging cysteines), indicating a Ni(III) $d_{z^2}$ ground state with the $C_\infty$ symmetry axis of the $d_{z^2}$ orbital parallel to this bond direction.

Spin density distributions for the paramagnetic states of [NiFe]-hydrogenases have been calculated by several groups using density functional theory (DFT) [16, 24, 25]. Although disagreement exists over the interpretations of certain aspects of the calculations, the overall spin density distribution in all calculations is compatible with the direction of the $d_{z^2}$ $C_\infty$ symmetry axis, as was found in the single crystal EPR study [23].

In parallel to our EPR study, the orientation of the *g*-tensor of the Ni-C state of two other enzymes, the [NiFe]-hydrogenase of *D. gigas* and the [NiFeSe]-hydrogenase of *D. baculatum*, which has a selenocysteine as a ligand to Ni, was indirectly determined from orientation-selected $^1H$ ENDOR spectroscopy on frozen solutions [26]. In this study, a comparison of the $^1H$ ENDOR signals from these two enzymes was performed and it was found that the ENDOR signals from both enzymes were very similar, which led to the conclusion that the active sites of the two proteins are essentially identical. Nevertheless, the *g*-tensor elucidated from these data differs significantly from the one for *D. vulgaris* Miyazaki F and from the ones calculated by DFT on a [NiFe]-hydrogenase model system. The $g_z$ principal axis (called $g_3$ in reference [23]) is found to make an angle of 37° with the Ni-S (Cys 549) (Cys-533 for *D. gigas*) direction [26]. An angle of only 5° was found for Ni-C in *D. vulgaris* Miyazaki F [23]. The orientations of the $g_x$ and $g_y$ axes differ by more than 50° in these studies.

In order to obtain more detailed information about the electronic structure of the Ni-C state and to solve this discrepancy we performed orientation-selected $^1H$ ENDOR spectroscopy and HYSCORE spectroscopy on *D. vulgaris* Miyazaki F [NiFe]-hydrogenase. Proton hyperfine couplings were deduced for three non-exchangeable protons from ENDOR. HYSCORE spectroscopy showed that the hydride bridge, as found for the regulatory hydrogenase of *R. eutropha*, is also present in the standard hydrogenases. The results are compared to those obtained for *D. gigas* hydrogenase and those derived from DFT calculations to obtain a consistent picture of the electronic structure of the reduced Ni-C state.

## Materials and methods

### Sample preparation

The [NiFe]-hydrogenase from *D. vulgaris* Miyazaki F was isolated and purified as described previously [27]. Tris/HCl buffer for the solvent exchange was prepared by thorough lyophylization of 1 ml portions of the respective buffer solution in $H_2O$ and redilution in the solvent. To achieve 25 mM Tris/DCl $pD_{true} = 7.4$, a dried solution of Tris/HCl at pH 7.1 was used [28, 29]. Solvent exchange to $D_2O$ (99.9 atom %) was achieved by concentrating the enzyme solution with a microconcentrator to about 1/20 of the initial volume and rediluting it six times at 5 °C with the respective buffer solution in $D_2O$.

*Desulfovibrio vulgaris* hydrogenase samples were equilibrated in the EPR tubes in a pure hydrogen gas atmosphere for 2–3 h, yielding the Ni-C state. Samples with an increased fraction of the "unsplit" Ni-C form were generated by purging the reduced enzyme for 15–30 min with argon as described in [30]. The fraction of unsplit Ni-C was estimated to be 50–70% according to the relative intensities of the EPR signals of the split and unsplit form at $g_y$ and $g_x$. Reduction of the enzyme in $D_2O$ was undertaken in 100% $D_2$ gas atmosphere following the procedure described above.

### EPR, ENDOR, and HYSCORE spectroscopy

EPR spectra were measured on a Bruker ESP 300E spectrometer equipped with a Bruker 4105 DR resonator. The cw-ENDOR measurements were performed on the same type of spectrometer using a home-built $TM_{110}$ ENDOR resonator especially designed for low-temperature experiments on transition metal systems [31]. A 16-turn ENDOR coil was used for the $^1H$ ENDOR experiments. Furthermore, a radio frequency (RF) signal generator (Rhode-Schwarz, SMT 02), and a 200 W RF power amplifier (ENI A3200 L, 0.25–150 MHz) were employed. Both set-ups were equipped with an Oxford helium cryostat ESR 910 (1.8–300 K), the field was calibrated with a Bruker ER035 NMR-Teslameter and the microwave frequency was measured with a Hewlett-Packard 5352B frequency counter.

Pulse EPR and HYSCORE measurements were performed with a Bruker ESP 380E spectrometer in a Bruker dielectric ring resonator (ESP380-1052 DLQ-H) equipped with an Oxford helium cryostat CF 935. Temperatures below 4.2 K were obtained by decreasing the pressure in the cryostat with an additional pump. In the 2D-HYSCORE experiment, the pulse sequence of $\pi/2$-$\tau$-$\pi/2$-$t_1$-$\pi$-$t_2$-$\pi/2$-$\tau$-*echo* [32, 33] was applied with $\pi/2$ and $\pi$ pulses of 16 and 32 ns, respectively. A four-step phase cycle suggested by Gemperle et al. [34] was used to eliminate contributions from unwanted echoes from the echo envelopes. The baseline of the 2D modulation pattern was subtracted using a second-order polynomial background function. Subsequently, the time traces were multiplied with a Hamming function and zero-filled to 512×512 points. The data were then Fourier-transformed to obtain magnitude contour spectra.

### Simulation procedures

The EPR powder spectra were simulated using an in-house simulation program [35]. Orientation-selected ENDOR spectra were simulated using the program SPLEEN [36]. This program computes ENDOR transition frequencies and intensities for an arbitrary number of paramagnetic nuclei, performing a full diagonalization of the nuclear spin Hamiltonian. The intensity of an ENDOR transition was assumed to be proportional to that of the EPR transition. A more detailed description of the simulation program is available in [36]. For a nucleus with $I = 1/2$, six parameters are required to specify the hyperfine tensor: the isotropic hfc ($a_{iso}$), two anisotropic hfc's, and furthermore three Euler angles, relating the orientation of the principal axes of the hyperfine tensor to that of the *g*-tensor. Initial values for the Euler angles were calculated as follows. The coordinates of the $\beta$-$CH_2$ protons of all coordinating cysteines in the X-ray structure of the reduced enzyme [18] were calculated. Then the Ni-H vectors were calculated, which were taken as a rough estimate for the direction of the dipolar hyperfine axis. These directions were transformed from the crystallographic axes system into the *g*-tensor axes system by making use of our knowledge of the complete *g*-tensor from single crystal EPR spectroscopy [23]. The simulations were subsequently optimized by fitting the six parameters to the signals observed in the experimental ENDOR spectra, whereby each ENDOR transition was assigned a fixed line width of 380 kHz in the simulation. Following the optimization, the hyperfine tensors were transformed back to the crystallographic axes system. It should be noted that the principal axes of the hyperfine tensors can be rotated by 180° about the *g*-tensor principal axes without affecting the simulation. This means that there are four possible choices for the directions of the axes, related by 180° rotations around the principal axes of the *g*-tensor, which give identical ENDOR simulations.

Simulations of the HYSCORE spectra were performed using a simulation program previously employed for ESEEM simulations [37] in which the HYSCORE modulation formula [33] was incorporated. This performs a full diagonalization of the nuclear spin Hamiltonian. When more than one nuclear spin interacts with the electron spin, the nuclear spin Hamiltonian is diagonalized separately for each nucleus and the modulation function is obtained from the product rule [38]. The amplitudes are calculated from the eigenvectors of the nuclear spin Hamiltonian. The program computes the spectrum at a given magnetic field and microwave frequency by considering only those molecules for which

the orientation is such that the effective $g$ value fulfills the resonance condition. This is the case when the effective $g$ value of the particular orientation and the $g$ value determined by the fixed magnetic field and microwave frequency are close to each other. In this procedure, the linewidth parameters of the EPR spectrum are used as a criterion, where it was assumed that the linewidth tensor is collinear with the $g$-tensor. Then, for each nucleus, six parameters are needed to specify the hyperfine tensor, and for nuclei with $I > 1/2$, five additional parameters for the (traceless) quadrupole tensor. For deuterium (in the bridging position between Ni and Fe), initial values for the hyperfine parameters $a_{iso}$ and dipolar part of the anisotropic tensor ($a_{dip}$) were determined from the HYSCORE spectra according to the method described by Pöppl et al. [39]. This procedure is feasible since three out of four $^2$H cross peaks do not overlap with other signals. For nitrogen, initial values for the quadrupole parameters $e^2\,qQ/h$ and $\eta$ can be derived from the frequencies that correspond to the nuclear quadrupole transitions (see below). The transitions were assigned a linewidth of 110 kHz. After considering all possible orientations (an equally-spaced grid with 200 steps for the polar angle $\theta$ was used), the 2-D array can be directly compared with the experimental spectrum.

For $^{14}$N, strong modulations are observable when the nuclear Zeeman and hyperfine terms cancel each other in one $M_S$ manifold ($|A| = 2\nu_n$). Then, only the nuclear quadrupole transitions $\nu_+$, $\nu_-$, $\nu_0$ are observed ($\nu_+ = \nu_- + \nu_0$), yielding sharp lines with strong intensities. They are related to the principal values of the traceless quadrupole tensor, expressed by the parameters $K$ and $\eta$: $K = e^2qQ/4h = (\nu_+ + \nu_-)/6$, $\eta = 3\nu_0/(\nu_+ + \nu_-)$. From the other $M_S$ manifold a (broader) double quantum transition $\nu_{DQ}$ is usually observed from which the effective hfc can be obtained: $\nu_{DQ} = 2\,[(\nu_n \pm |A|/2)^2 + \xi^2]^{1/2}$ with $\xi = K(3+\eta^2)^{1/2}$ [38, 40]. In HYSCORE spectra, correlation frequencies are expected for $^{14}$N between $\nu_{DQ}$ and any of the three frequencies ($\nu_0$, $\nu_+$, $\nu_-$) of the other $M_S$ manifold.

Simulations are performed for the HYSCORE part (off-diagonal part) of the spectrum only. No attempts have been made to simulate the signals on the diagonal, which result from the stimulated (three pulse) echo and incomplete population inversion by the microwave $\pi$ pulse.

## Results

### EPR spectroscopy

The continuous-wave (cw) EPR spectra for the reduced Ni-C state of *D. vulgaris* Miyazaki F hydrogenase in $H_2O$ and in $D_2O$ measured at 50 K are shown in Fig. 2a, b respectively. Simulations of the spectra are also included and simulation parameters are given in Table 1. The Ni-C state is characterized by $g$ values that are compatible with those found by other groups for similar [NiFe]-hydrogenases [20, 21, 26, 30, 41, 42] and characteristic for a Ni(III) state where the unpaired electron is mainly in a $d_{z^2}$ orbital of nickel. A narrowing of the linewidths at all canonical orientations is observed upon solvent exchange to $D_2O$ and subsequent reduction of the sample with $D_2$. The most pronounced narrowing is present at the $g_y$ orientation, for which the linewidth (peak-to-peak) reduces from 2.15 to 1.67 mT. This line-narrowing largely results from the exchange of a hydride directly bound to the [NiFe] center, as was deduced from earlier observations with ENDOR and HYSCORE spectroscopy [20, 22], the magnitude of the hyperfine coupling being on the order of 20 MHz. A similar line-narrowing upon $D_2O$ exchange has recently been observed by Müller et al. [26] for *D. gigas* hydrogenase.

When the proximal [4Fe4S] cluster is paramagnetic and the temperature is lowered to below 40 K, the Ni-C

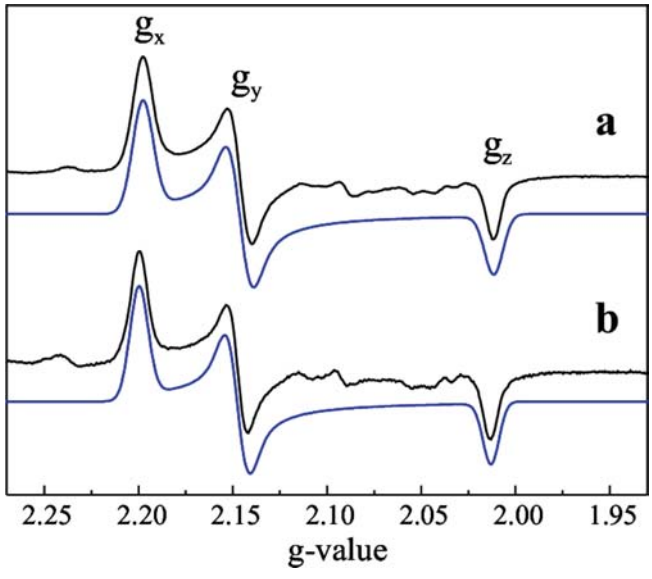


**Fig. 2** X-band EPR spectra of the Ni-C state of the [NiFe]-hydrogenase of *D. vulgaris* Miyazaki F at $T = 50$ K in $H_2O$ (*a*) and $D_2O$ (*b*). The principal values of the $g$-tensor are indicated. The simulations (*blue lines*) were obtained by using the parameters in Table 1. Experimental conditions: $\nu_{mw} = 9.60$ GHz, $P_{mw} = 1.0$ mW, modulation amplitude = 0.28 mT

**Table 1** $g$-Tensor principal values $g_i$ ($i = x, y, z$) and linewidth parameters $w_i$ (mT) of the Ni-C state of *D. vulgaris* Miyazaki F [NiFe]-hydrogenase at $T = 50$ K

| Solvent | $g$ values | | | Linewidths (mT) | | |
|---|---|---|---|---|---|---|
| | $g_x$ | $g_y$ | $g_z$ | $w_x$ | $w_y$ | $w_z$ |
| $H_2O$ | 2.196 | 2.145 | 2.010 | 2.05 | 2.15 | 1.95 |
| $D_2O$ | 2.198 | 2.146 | 2.011 | 1.67 | 1.67 | 1.67 |

Error margins are $\Delta g = 0.003$ and $\Delta w = 0.05$ mT. Linewidth measured as full-width-half-maximum ($w_x$, $w_z$) or peak-to-peak ($w_y$)

EPR signal broadens. Below 12 K the signal splits, which is a result of spin–spin interaction between the [NiFe] and proximal [4Fe4S] centers [30, 43]. The splitting of the Ni-C EPR signal can be largely avoided by setting the redox potential such that the [4Fe4S] clusters are oxidized. The mid-point potential of the Ni-C state happens to be close to that of the [4Fe4S] clusters of the small subunit [6, 29, 44, 45]. For *D. vulgaris* Miyazaki F hydrogenase the redox potential was carefully chosen such that 50–70% of the [4Fe4S] clusters were in the oxidized state (see "Materials and methods" section).

## Orientation-selected ENDOR spectroscopy

Initial cw and pulse ENDOR experiments on samples which exhibit a completely split Ni-C EPR spectrum were not successful. No ENDOR effect was observed because of the enhanced relaxation rate caused by the interaction with the paramagnetic proximal [4Fe4S] cluster. By making use of carefully prepared Ni-C samples in which the potential was set such that the [4Fe4S] clusters remained largely oxidized, unsplit Ni-C EPR signals could be obtained in high quantity (50–70%). With a ratio of split:unsplit Ni-C of roughly 1:2, cw-ENDOR signals could be observed. However, pulse ENDOR signals remained difficult to obtain, most probably because the nuclear relaxation is still faster than the timescale of the pulse ENDOR experiment. The cw-ENDOR effect of this sample is weak and only high enzyme concentrations (~2 mM) and prolonged accumulation times (~3–12 h) led to acceptable signal-to-noise ratios. The optimal signal-to-noise ratio was obtained at a temperature of 25 K.

A set of orientation-selected ENDOR spectra for the hydrogenase in $H_2O$ is shown in Fig. 3. The effective $g$ value is indicated to the right of each spectrum. The spectra reveal an intense transition at the $^1H$ Zeeman frequency, $\nu_H$, which results from protons relatively distant from the [NiFe] center. Signals of lower intensity are observed at frequency shifts of up to 9 MHz. Almost all prominent signals are symmetrically displayed around $\nu_H$, with the signals on the high-frequency side of $\nu_H$ being more intense than those observed on the low-frequency side. The range of frequency shifts observed here is comparable to that observed in an earlier study by Müller et al. [26] on *D. gigas* [NiFe]-hydrogenase. Because of a better signal-to-noise ratio in their spectra, Müller et al. were able to observe more signals in this region.

For the analysis of the ENDOR spectra, a set of transitions had to be attributed to one distinct nucleus by tracing the positions of the transitions over the whole field range. In this procedure, signals from one proton have to be grouped together, which can be facilitated by means of a field-frequency plot (see Fig. 3, top). The three largest hyperfine couplings can be clearly distinguished in the ENDOR spectra of Ni-C. The signals belonging to these couplings are named **a**, **b** and **c**.

In a next step, the ENDOR signals were simulated. As starting parameters for the simulations, the maximum ($A_{||}$) and minimum ($A_{\perp}$) shift of the signals were read from the field-frequency plot. Using the axial hyperfine tensor to start with, the isotropic hyperfine coupling constant ($a_{iso} = 1/3(A_{||} + 2A_{\perp})$ and purely dipolar hfc $A_{\perp}' = 1/3(A_{\perp} - A_{||})$ were calculated. For the initial simulations, the orientation of the dipolar

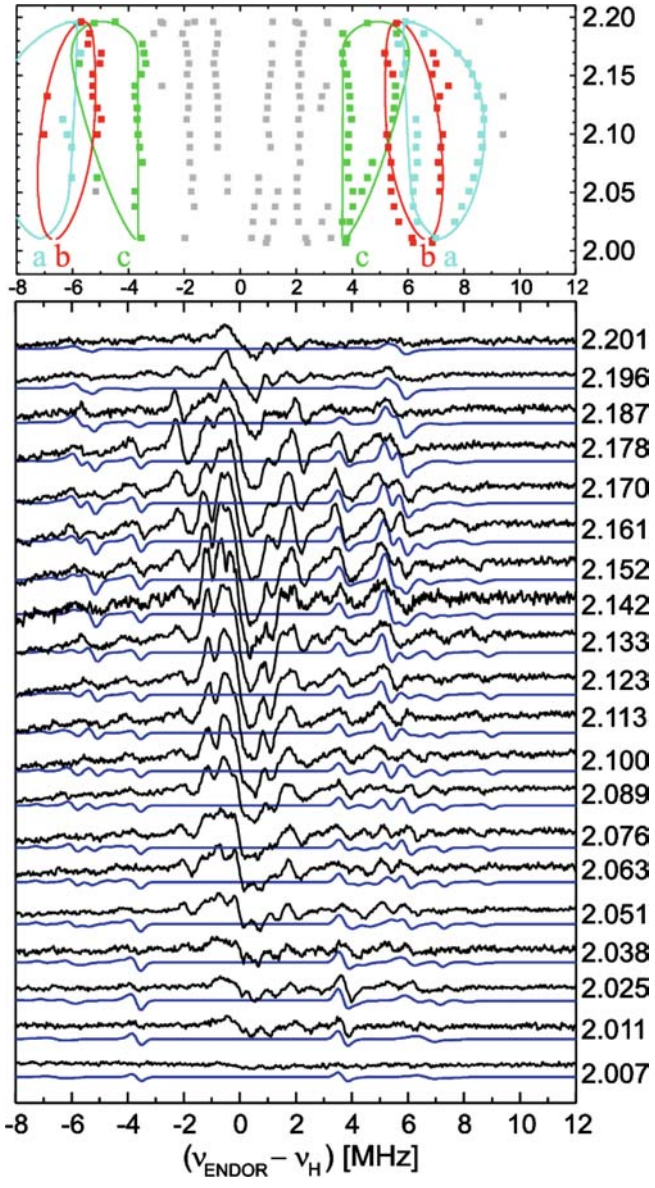


**Fig. 3** *Top*: field-frequency plot of the experimental Ni-C ENDOR spectra. The *colored lines* connect signals that belong to proton **a** (*blue*), **b** (*red*) or **c** (*green*). *Bottom*: orientation selected cw-ENDOR spectra for the Ni-C state of *D. vulgaris* Miyazaki F hydrogenase recorded at various effective $g$ values. Simulations of the ENDOR spectra are indicated by *blue lines*, see text and Table 2. Experimental conditions: $\nu_{mw} = 9.5$ GHz, $T = 25$ K, $P_{mw} = 30.2$ mW, RF frequency modulation 12.5 kHz, modulation amplitude 200 kHz, accumulation time for the individual spectra varies between 3 and 12 h, depending on the magnetic field setting

axes is also needed. For this purpose the positions of all $\beta$-$CH_2$ protons of the coordinating cysteine ligands were deduced using the X-ray structure of the reduced enzyme [18] and the Ni-H vectors were calculated as first estimates for the directions of the dipolar axes. Transformation of the vectors into the *g*-tensor principal axis system [23] yielded a set of Euler angles relating the directions of the dipolar axes to the principal *g*-tensor axes. Then it was tested which of the dipolar axes orientations, with the appropriate initial hyperfine parameters, reproduced the signals in the field-frequency plot best. After subsequent variation of all the parameters—first optimizing the simulation at the single crystal-like positions, $g_x$ and $g_z$, and then for the intermediate field positions, and finally relaxing the restriction of axially symmetric hyperfine tensors—a good simulation of the ENDOR spectra and an estimate for the errors of the individual adjustable parameters was obtained. The resulting simulations are included in Fig. 3 (bottom) and the hyperfine coupling constants are summarized in Table 2. The ENDOR simulations are insensitive to 180° rotations of the principal axes of the hyperfine tensor about any of the principal axes of the *g*-tensor.

It is apparent from Fig. 3 that the signals assigned to protons **a**, **b** and **c** are well simulated. Furthermore, the signals of protons **a** and **b** have the largest frequency shift and they behave similarly when the magnetic field setting is changed. From the simulation of these signals relatively large isotropic hyperfine interactions of 13.7 and 11.8 MHz are elucidated, which is an indication that these signals do indeed originate from the $\beta$-$CH_2$ protons of one cysteine residue carrying a large fraction of the spin density. The signals of proton **c** have a smaller shift than those of protons **a** and **b**. Proton **c** is also characterized by a hyperfine tensor, which is dominated by the isotropic coupling constant (8.9 MHz), and the anisotropic part is comparable in size to those of protons **a** and **b**.

Additionally, experiments were performed on samples in $D_2O/D_2$ and orientation-selected ENDOR spectra were recorded at 17 magnetic field positions. The spectra (data not shown) looked very similar to those in $H_2O/H_2$ with only minor intensity changes. The signals of protons **a**, **b** and **c** are clearly observable in these spectra, indicating that these protons are not exchangeable.

**Table 2** $^1$H hyperfine coupling tensor components $A_i$ ($i = x, y, z$) (MHz) and direction cosines $l_{ai}$, $l_{bi}$, $l_{ci}$ with respect to the crystallographic axes (*a*, *b*, *c*) for the protons **a**, **b** and **c** of *D. vulgaris* Miyazaki F hydrogenase in the Ni-C state, as determined from simulations of the ENDOR spectra (see Fig. 3). Also included is the isotropic hyperfine coupling constant $a_{iso}$ (MHz) and the purely dipolar hyperfine coupling tensor components $A_i'$ (MHz)

| Proton | Parameter | *x* | *y* | *z* | Assignment |
|---|---|---|---|---|---|
| **a** | $a_{iso}$ | | 13.7 | | Cys-549 ($\beta$-$CH_2$) |
| | $A_i$ | −1.8 | −2.4 | 4.2 | |
| | $A_i$ | 11.9 | 11.3 | 17.9 | |
| | $l_{ai}$ | 0.58 | −0.49 | 0.65 | |
| | $l_{bi}$ | 0.74 | 0.65 | −0.17 | |
| | $l_{ci}$ | −0.33 | 0.58 | 0.74 | |
| **b** | $a_{iso}$ | | 11.8 | | Cys-549 ($\beta$-$CH_2$) |
| | $A_i$ | −1.1 | −1.5 | 2.7 | |
| | $A_i$ | 10.7 | 10.3 | 14.5 | |
| | $l_{ai}$ | (−0.74) | (0.18) | 0.65 | |
| | $l_{bi}$ | (−0.06) | (−0.98) | 0.21 | |
| | $l_{ci}$ | (0.67) | (0.12) | 0.73 | |
| **c** | $a_{iso}$ | | 8.9 | | Cys-546 ($\beta$-$CH_2$) |
| | $A_i$ | −1.6 | −1.6 | 3.1 | |
| | $A_i$ | 7.3 | 7.3 | 12.0 | |
| | $l_{ai}$ | | | −0.09 | |
| | $l_{bi}$ | | | −0.49 | |
| | $l_{ci}$ | | | 0.87 | |

The estimated error margin for $A_i$ is ±0.3 MHz, that for the directions of the principal axes is ±15°, except the values in brackets. These have a larger error margin (±30°) because of the near-degeneracy of the principal values

## HYSCORE spectroscopy

Figure 4a, b depict the HYSCORE spectra of the Ni-C state of *D. vulgaris* Miyazaki F hydrogenase in $H_2O$ and $D_2O$ in the low-frequency regime. The spectra are dominated by strong signals on the diagonal, which stem from the stimulated (three pulse) echo. In the spectrum in $H_2O$, three signals at 0.5, 1.2 and 1.7 MHz are present, indicated with blue dots. Such a pattern, where the two smallest frequencies add up to the largest frequency, indicates that these signals stem from one nucleus with $I = 1$ (nitrogen). Under the "exact cancellation" condition [40], the nuclear Zeeman interaction and hyperfine interaction cancel each other in one of the $M_S$ manifolds and the three frequencies $\nu_+$, $\nu_-$ and $\nu_0$ are determined by the quadrupole interaction of this nucleus. Additional signals on the diagonal are found at 2.3 and 3.5 MHz. At 3.9 MHz an artifact from the spectrometer related to the 125 MHz clock frequency of the pulse programmer appears. Cross peaks of lower intensity are observed in the spectrum in $H_2O$, which relate the nitrogen single-quantum frequencies of 1.2 and 1.7 MHz to a broad double-quantum transition between 4 and 5 MHz (cross peak labeled (i), refer to Fig. 1). Cross peaks (ii) also relate the peak at 2.3 MHz to about 3.9 MHz. These frequencies probably also stem from nitrogen (vide infra).

Upon $H_2O \rightarrow D_2O$ exchange of the solvent, additional cross peaks become visible in Fig. 4b. These cross peaks are only marginally above the noise level (indicated in red in the figure). The first one lies close to the Zeeman frequency of deuterium (2.1 MHz) and extends up to 1 MHz away from the diagonal. A similar peak, albeit one with even less intensity, is present at exactly double the frequency. In addition, a "v" shaped cross peak appears, which starts at approximately 3.2 MHz and ends at (5.5, 2.6) MHz and (2.6, 5.5) MHz. Note that the relaxation properties of the spin system reacted sensitively on $H_2O \rightarrow D_2O$ solvent exchange, and the nitrogen couplings are more pronounced in the HY-

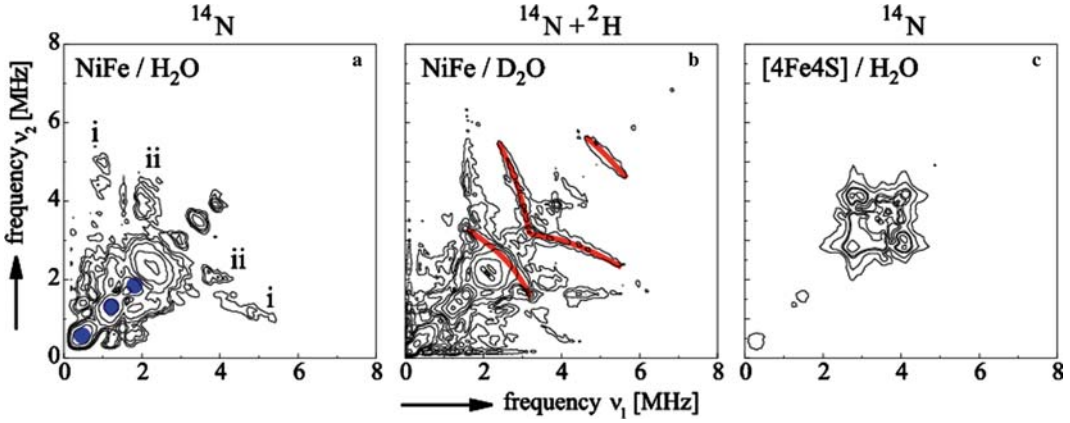


**Fig. 4a–c** HYSCORE spectra ($^{14}$N/$^{2}$H region) for the Ni-C state of *D. vulgaris* Miyazaki F hydrogenase in $H_2O$ (**a**) and $D_2O$ (**b**), recorded at the $g_y$ canonical orientation ($B_0 = 325.0$ mT). Experimental conditions: $\nu_{mw} = 9.7$ GHz, $T = 3.1$ K, length of 90° pulse 16 ns, $\tau_1 = 120$ ns, $\tau_2 = 160$ ns, $\tau_3 = 200$ ns (addition of three spectra). Steps of $t_1$ and $t_2$ 16 ns, resolution 256×256 data points, accumulation time ~5 h per spectrum. Also included is a HYSCORE spectrum of the reduced [4Fe4S] clusters in $H_2O$ (**c**), recorded at $B = 345.1$ mT, $\tau = 120$ ns. All signals in **a** belong to nitrogen, while in **b** additional signals from $^{2}$H (indicated in *red*) are superimposed. The *blue dots* in **a** indicate intense lines on the diagonal belonging to zero field frequencies $\nu_0$, $\nu_-$, $\nu_+$ of the $^{14}$N. In **a** the labels *i* and *ii* indicate cross peaks between $\nu_{DQ}$ and one of the single quadrupole frequencies $\nu_+$ and $\nu_-$ (see text)

SCORE spectra of the $D_2O$ sample. Differences in relaxation rates have been observed before in ENDOR spectra of hydrogenases [20, 21].

For comparison, an additional HYSCORE spectrum was recorded at a magnetic field setting where only the [FeS] clusters contribute to the EPR spectrum (Fig. 4c). It should be clearly noted that the [4Fe4S] clusters, when they are reduced as is the case for split Ni-C, give rise to a pulse EPR signal which overlaps with that of the [NiFe] center over the entire field-range spanned by the $g$ values of Ni-C. The HYSCORE spectrum for the [FeS] clusters was recorded at a magnetic field setting which is marginally larger than the one that corresponds to the $g_z$ value of the Ni-C state. In this spectrum, the strong diagonal peaks indicated by the blue dots disappeared, indicating that they belong to a nitrogen associated with the [NiFe] center, but the intensity remains in the area between 2.5 and 4.5 MHz. A pattern like this, where only the nuclear double-quantum transitions of both $M_S$ manifolds are present, is indicative of a nitrogen for which the exact cancellation condition [40] is not fulfilled. As both the proximal and distal [4Fe4S] cluster are coordinated by a histidine (His 235 for the proximal cluster and His 188 for the distal cluster), it is likely that these signals are related to these residues and not to a nitrogen near the [NiFe] center. Lastly, the signals indicated in red in the spectrum in $D_2O$ (Fig. 4b) have also disappeared in Fig. 4c, indicating that these signals are related to the [NiFe] center. The pattern marked with the blue dots at 0.5, 1.2 and 1.7 MHz (Fig. 4a) is indicative of a histidine nitrogen [46, 47] and we therefore assign this pattern to the $\epsilon$ nitrogen of histidine-88 of the large subunit, which forms a hydrogen bond to the Cys-549 of the [NiFe] center.

In a next step, the signals associated with the [NiFe] center (the nitrogen and deuterium signals) were simulated. A single HYSCORE spectrum recorded at $g_y$ and $\tau = 200$ ns is shown in Fig. 5a. The deuterium signals are very similar to those found recently for the Ni-C state of the regulatory hydrogenase of *R. eutropha* [22]. The latter

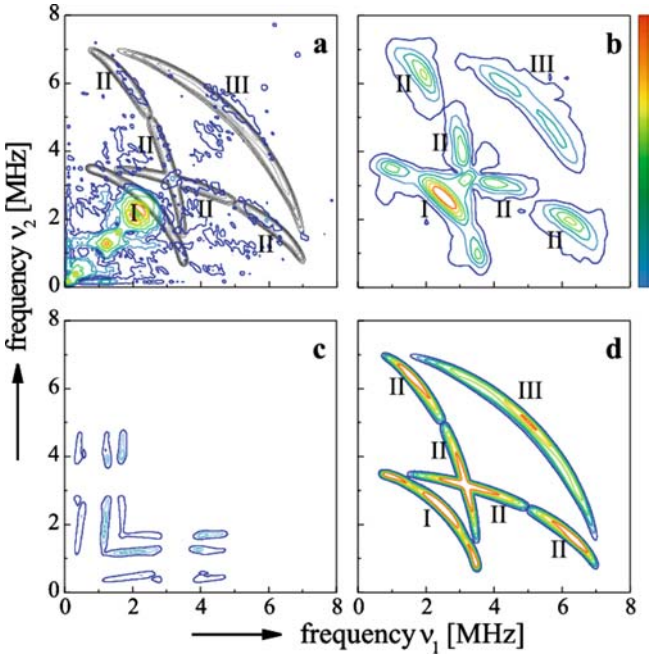


**Fig. 5a–d** HYSCORE spectra ($^{14}$N/$^{2}$H region) for **a** Ni-C of *D. vulgaris* Miyazaki F hydrogenase in $D_2O$ at the $g_y$ canonical orientation ($\nu_{mw} = 9.7$ GHz, $\tau = 200$ ns, $B_0 = 325.0$ mT, length of the 90° pulse 16 ns), and **b** Ni-C of the regulatory hydrogenase of *R. eutropha*, reproduced from [22]. Also included is a simulation for a nitrogen nucleus, assigned to the $N_\epsilon$ of histidine-88 [47] (**c**) and a simulation for the deuterium bridging ligand (**d**) (see [22]). The simulation for the deuterium bridging ligand in *D. vulgaris* Miyazaki F, which is very similar to that of *R. eutropha* is superimposed in *gray* in **a**

enzyme has the advantage that the [4Fe4S] clusters remain oxidized when the [NiFe] center is in the Ni-C state, and experiments at low temperatures are therefore possible due to the absence of the spin–spin interaction of the [NiFe] center and the proximal [4Fe4S] cluster. Furthermore, the histidine, which forms a hydrogen bond to one of the Ni-coordinating sulfurs in *D. vulgaris*, is not present in this enzyme, and therefore nitrogen contributions are absent in the HYSCORE spectrum of *R. eutropha*. The HYSCORE spectrum of this enzyme in $D_2O$, recorded under the same conditions, is reproduced in Fig. 5b. It is apparent that the signal-to-noise ratio is much better than that of Fig. 5a. Nevertheless, the deuterium signals can clearly be seen in both spectra. Cross peak I corresponds to correlations between the single-quantum transitions of both $M_S$ manifolds, cross peak II (the "v" shaped cross peak in Fig. 4) to correlations between a single quantum transition of one $M_S$ manifold with the double quantum transition of the other $M_S$ manifold, and cross peak III to correlations between the double quantum transitions of both $M_S$ manifolds.

Although the signal-to-noise ratios differ, the deuterium signals in Fig. 5a could be analyzed and are found to be almost the same as in Fig. 5b. Therefore, HYSCORE simulations were performed with the same parameters as those used for the deuterium nucleus of *R. eutropha*. The parameters are given in Table 3 and the simulation is shown in Fig. 5d, where it is seen that all deuterium-related signals of the experimental spectra are reproduced well by the simulations. It should be noted that the quadrupole splitting for deuterium ($\lessapprox$100 kHz) [22] is smaller than the observed linewidth. In order to keep the number of parameters to a minimum, the quadrupole interaction has therefore been neglected in the simulation.

Since the correlation frequencies of the nitrogen are poorly resolved in the experimental spectra, severe limitations have been placed on the number of free parameters in the simulation procedure. First, from the three single-quantum frequencies on the diagonal (see Fig. 4a), the quadrupole parameters have been estimated using the formulae given in "Materials and methods". The double quantum frequency of nitrogen is broad and spans a range from 4 to 5 MHz, as seen from the signal on the diagonal at 4.5 MHz and from the cross peaks at (4.5, 0.5) MHz and (1.6, 4.5) MHz. From this, starting values for the isotropic hyperfine coupling constant $a_{iso}$ and dipolar constant $A_x'$ were obtained. The hyperfine tensor was restricted to being axial. The principal axes were kept fixed to the following directions based on the crystal structure [18]: the $x$-axis of the hyperfine tensor (dipolar axis) was chosen parallel to the $N_\epsilon$-H (His 88) direction, which also points to the large spin density on the $S_\gamma$ of Cys-549 [25]. The quadrupole $x$-axis was also parallel to the $N_\epsilon$-$H_\epsilon$ direction, the $y$-axis perpendicular to the imidazole plane, and the $z$-axis was tangential to the imidazole [46]. With these initial parameters, the simulations were optimized by changing only $a_{iso}$, $A_x'$ and $e^2\ qQ/h$. Optimized parameters are given in Table 4 and the resulting simulation is shown in Fig. 5c. The modulation depth is similar to that of the deuterium nucleus (Fig. 5d), but for a better comparison with the experimental spectrum, the contour levels have been chosen differently.

The simulation shows 12 cross peaks (Fig. 5c). Unlike for the deuterium, these cross peaks are directed either horizontally or vertically in the spectrum. The reason for this is that the single quantum transitions of the cancelled $M_S$ manifold are largely determined by the nuclear quadrupole interaction, which does not vary with field. In general, the presence of horizontally - or vertically - oriented cross peaks in the low-frequency region of HYSCORE spectra is indicative of nitrogen. The six horizontal (or vertical) cross peaks correlate the single quantum frequencies in the cancelled $M_S$ manifold with the double quantum frequency of the non-cancelled manifold [at (0.5, 4.4) MHz, (1.2, 4.4) MHz and (1.7, 4.4) MHz], and the single quantum frequencies in the cancelled manifold to the single quantum frequencies of

**Table 3** $^1$H hyperfine tensor components (MHz) and direction cosines with respect to the crystallographic axes ($a$, $b$, $c$) of the exchangeable proton of *D. vulgaris* Miyazaki F

| Parameter | $x$ | $y$ | $z$ |
|---|---|---|---|
| $a_{iso}$ | | −3.5 | |
| $A_i$ | 21.9 | −7.3 | −14.5 |
| $A_i$ | 18.4 | −10.8 | −18.0 |
| $l_{ai}$ | −0.63 | 0.54 | −0.55 |
| $l_{bi}$ | 0.21 | 0.81 | 0.55 |
| $l_{ci}$ | 0.74 | 0.23 | −0.63 |

The parameters were taken to be identical to the ones reported for the regulatory hydrogenase of *R.eutropha* [22]. For deuterium, the principal values must be scaled down by a factor $\gamma_N(^1H)/\gamma_N(^2H) = 6.51$

**Table 4** $^{14}$N hyperfine ($A_i$) and quadrupole ($P_i$) tensor components (MHz) for Ni-C in *D.vulgaris* Miyazaki F

| Parameter | $x$ | $y$ | $z$ |
|---|---|---|---|
| $a_{iso}$ | | 1.9 | |
| $A_i$ | 0.8 | −0.4 | −0.4 |
| $A_i$ | 2.7 | 1.5 | 1.5 |
| $l_{ai}$ | −0.34 | | |
| $l_{bi}$ | −0.90 | | |
| $l_{ci}$ | 0.28 | | |
| $e^2\ qQ/h$ | | 1.88 | |
| $\eta$ | | 0.40 | |
| $P_i$ | −0.28 | −0.66 | 0.94 |
| $l_{ai}$ | −0.34 | −0.84 | 0.41 |
| $l_{bi}$ | −0.90 | 0.44 | 0.12 |
| $l_{ci}$ | 0.28 | 0.32 | 0.90 |

The nitrogen is assigned to $N_\epsilon$ (His88) that is involved in a hydrogen bond to the sulfur of Cys549. Because of the low signal-to-noise ratio, the directions of the principal axes were kept fixed (see text) and the hyperfine tensor was restrained to being axial. The error margin for $a_{iso}$, $A_i$ and $e^2\ qQ/h$ is 0.2 MHz. (Note that the quadrupole coupling constant $e^2\ qQ/h = 2P_z$ (major component) and $\eta = (|P_y| - |P_x|)/|P_z|$)

the non-cancelled $M_S$ manifolds [at (0.5, ~2.0) MHz, (1.2, ~2.0) MHz and (1.7, ~2.0) MHz]. Although good agreement cannot be expected due to the low signal-to-noise ratio of the experimental spectrum, the most intense cross peaks of the simulation (Fig. 5c) can easily be found in Fig. 5a.

## Discussion

In the discussion, we first focus on the assignment of the signals in the ENDOR spectra to non-exchangeable protons of cysteine ligands of the [NiFe] center. Secondly, the signals in the HYSCORE spectrum in $D_2O$ will be assigned based on comparison with data for the Ni-C state of the regulatory hydrogenase of *R. eutropha* [22].

### Assignment of the non-exchangeable protons

In the field-frequency plot (Fig. 3, top) contributions from three protons (labeled **a**, **b** and **c**) are observed. Additional experiments following $D_2O$ exchange indicate that these protons belong to non-exchangeable protons. The shape of the curves which connect the resonances from the same proton are virtually identical to those observed earlier for *D. gigas* and *D. baculatum* hydrogenase [26]. In agreement with conclusions drawn in this work, our data confirm that the [NiFe] center is essentially the same in these enzymes, even up to the detailed nuclear resolution that can be addressed by orientation-selected ENDOR spectroscopy. The protons **a**, **b** and **c** of this work correspond well to protons named H-A, H-B and H-C in [26]. The large isotropic hyperfine interactions show that these protons belong to $\beta$ protons of the Ni-coordinated cysteines. Nevertheless, upon critical comparison, subtle differences can be found. For example, the field-frequency plot of *D. gigas* hydrogenase [26] reveals that the largest hyperfine coupling constant for the most strongly coupled proton (H-A) is about 18.5 MHz, whereas the plot for *D. vulgaris* hydrogenase (Fig. 3, top) shows that this constant is 17.9 MHz. Differences of the order of $\lessapprox$ 1 MHz are also found for the other hyperfine coupling constants determined from the simulations.

In order to assign the protons **a**, **b** and **c** to any of the $\beta$ protons of the Ni-coordinating cysteines, the directions of the principal axes of the hyperfine tensor with respect to those of the *g*-tensor are required. The directions follow directly from the simulation of the ENDOR spectra. We will mainly focus on the direction of the "dipolar axis", which corresponds to the largest principal value (the *z*-axis of the tensors of protons **a**, **b** and **c**). This direction is approximately parallel to the direction, which connects the location of the bulk spin-density (on nickel) and the position of the proton. Therefore, by using Ni-H starting vectors in the simulation program and combining them with knowledge of the *g*-tensor of the Ni-C state of *D. vulgaris* hydrogenase [23], good agreement was quickly found. The angle between the dipolar axis of proton **a** and the Ni-H vector for one of the $\beta$-protons of Cys-549 is 7°, the angle for proton **b** and the Ni-H vector of the other $\beta$-proton of Cys-549 is 6°, and the one for proton **c** and the Ni-H vector of a proton of Cys-546 is 12°. We therefore assign protons **a**, **b** and **c** to these $\beta$ protons, which is also intuitively expected since protons **a** and **b** show a similar behavior in the field-frequency plot (Fig. 3, top).

In Table 5, a detailed comparison is given between the hyperfine coupling parameters for *D. vulgaris* Miyazaki F and *D. gigas* hydrogenase, including the directions of the principal axes, which directly follow from the simulations. The simulations are, however, insensitive to 180° rotations of the hyperfine axes around any of the *g*-tensor axes (see Scheme 1 and "Materials and methods"). Neglecting the absolute signs of the direction cosines for a moment for the above reason, the largest angle between the dipolar axes for *D. vulgaris* and *D. gigas* hydrogenase occurs for proton **a** and amounts to 30°, which is about equal to the combined accuracy of both experiments. The angles are included in Table 5. We therefore conclude that the directions of the dipolar hyperfine axes of *D. vulgaris* and *D. gigas* hydrogenase, *neglecting the absolute signs* of the direction cosines, are similar. When our signs are taken for the direction cosines (see "Appendix") of the hyperfine axes of *D. gigas* hydrogenase [26], a similar assignment is obtained for this enzyme as well. In this case, the results from single crystal EPR data [23], from the ENDOR data presented here and in reference [26], and the DFT calculations for the Ni-C state are all in agreement. This result shows that the overall electronic structure of the [NiFe] center in the active Ni-C state is essentially the same in all [NiFe]-hydrogenases.

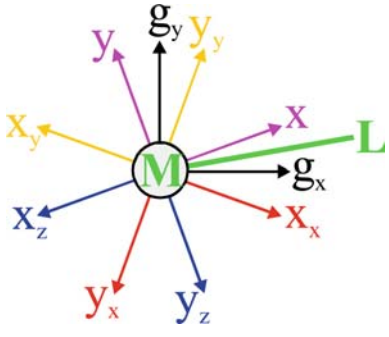


**Scheme 1** Illustration of the sign-ambiguity problem in ENDOR spectroscopy. The directions of the principal axes of the *g* tensor (with the *z*-axis chosen perpendicular to the plane of the paper) are shown in *black*, and those of the hyperfine tensor in *magenta* (for simplicity the hyperfine *z*-axis is also perpendicular to the plane of the paper). Other orientations of the hyperfine tensor, which give exactly the same field-frequency dependence in ENDOR spectroscopy, can be obtained by 180° rotations about any of the *g* tensor axes and are indicated in *red*, *yellow* and *blue*. It is then clear that the angles with the metal-ligand direction (indicated as M–L; for example Ni–H) can be different for all four possibilities

### Assignment of the exchangeable proton

The deuterium signals observed in the HYSCORE spectrum of *D. vulgaris* Miyazaki F (see Fig. 5a) look the same as those for the regulatory hydrogenase of *R. eutropha* (Fig. 5b). This is the first observation of these signals for a catalytically active hydrogenase. The regulatory hydrogenase does not exhibit split Ni-C signals and a hydrogen-bonded histidine to one of the Ni coordinating cysteines is absent. The simulation presented in Fig. 5d is performed with the hyperfine parameters of *R. eutropha* hydrogenase. Since the analysis is identical to the one presented for the regulatory hydrogenase, we refer to [22] for details. These signals were assigned to a formal hydride ($^1H^-/^2H^-$) located in the bridging position between Ni and Fe [22, 23]. The signals in Fig. 5a show that a hydride bridge is also present in the Ni-C state of the catalytic hydrogenase of *D. vulgaris* Miyazaki F. The hydride is bound in the equatorial plane of the $d_{z^2}$ orbital, which explains the small and negative isotropic hyperfine coupling constant; a result that is in full agreement with DFT calculations [25], see Table 6. Further smaller deuterium couplings are not resolved due to the presence of nitrogen signals in the same frequency region. The observation of the deuterium HYSCORE signals in both a regulatory and a catalytic hydrogenase suggests that the electronic structures of the [NiFe] centers in these proteins are also very similar and that differences in their activity most probably arise from effects located further away from the [NiFe] center.

## Summary and conclusion

Detailed information about the spin density distribution of the [NiFe] center has been obtained by applying both orientation-selected ENDOR and complementary HYSCORE spectroscopy to [NiFe]-hydrogenase frozen solutions. Knowledge of the orientation of the *g*-tensor, determined earlier through EPR studies of hydrogenase single crystals [23], was a prerequisite for the analysis.

The detection of H/D-exchangeable deuterium signals in the HYSCORE spectra of the Ni-C state of hydrogenase, as found earlier in a regulatory hydrogenase [22], provides direct experimental evidence for the

**Table 5** Comparison of $^1H$ hyperfine coupling constants (MHz) and direction cosines for the protons **a**, **b** and **c** of *D. vulgaris* Miyazaki F [NiFe]-hydrogenase and protons H-A, H-B and H-C for *D. gigas* hydrogenase (reproduced from [26]) with respect to the principal axes of the *g*-tensor ($i = x, y, z$). The direction cosines are given in the *g*-tensor frame [23]. Also included is the angle $\Theta_{gv}$ between the dipolar axes *z* for *D. gigas* and *D. vulgaris* Miyazaki F, while the signs of the direction cosines for *D. gigas* hydrogenase are taken as equal to those for *D. vulgaris* Miyazaki F

| Proton | *D. vulgaris* | | | | | | Proton | *D. gigas* | | | | | | |
|---|---|---|---|---|---|---|---|---|---|---|---|---|---|---|
| | $a_{iso}$ | | $A_i$ | $l_{(gx)i}$ | $l_{(gy)i}$ | $l_{(gz)i}$ | | $a_{iso}$ | | $A_i$ | $l_{(gx)i}$ | $l_{(gy)i}$ | $l_{(gz)i}$ | $\Theta_{gv}$ |
| **a** | 13.7 | *x* | 11.9 | −0.402 | 0.456 | 0.790 | H-A | 13.8 | *x* | 12.28 | −0.205 | −0.817 | 0.539 | |
| | | *y* | 11.3 | −0.860 | −0.482 | 0.165 | | | *y* | 10.66 | 0.789 | −0.471 | −0.395 | |
| | | *z* | 17.9 | 0.305 | −0.745 | 0.592 | | | *z* | 18.51 | −0.605 | −0.354 | −0.713 | 30 |
| **b** | 11.8 | *x* | 10.3 | 0.179 | 0.899 | 0.409 | H-B | 12.5 | *x* | 10.33 | 0.283 | 0.631 | 0.723 | |
| | | *y* | 10.7 | −0.908 | −0.003 | 0.420 | | | *y* | 11.33 | −0.819 | 0.552 | −0.157 | |
| | | *z* | 14.5 | 0.374 | −0.444 | 0.814 | | | *z* | 15.83 | 0.521 | 0.560 | −0.645 | 14 |
| **c** | 8.9 | *x* | 7.3 | | | | H-C | 8.9 | *x* | 6.78 | −0.165 | 0.373 | −0.913 | |
| | | *y* | 7.3 | | | | | | *y* | 7.44 | 0.619 | −0.693 | −0.369 | |
| | | *z* | 12.0 | −0.693 | 0.714 | 0.125 | | | *z* | 12.35 | −0.778 | −0.618 | −0.107 | 1 |

**Table 6** Calculated $^1H$ hyperfine coupling constants (MHz) and directions of the principal axes ($i = x, y, z$) for the strongly coupled protons of a Ni-C model for [NiFe]-hydrogenase (see [25]). The direction cosines are given in the *g*-tensor frame [23]. Also included are the angles $\phi_v$ and $\phi_g$ (deg) between the calculated and experimental (see Table 5) dipolar principal hyperfine axes *z* for *D. vulgaris* Miyazaki F and *D. gigas* hydrogenase, respectively. For the bridging $H^-$, only $\phi_v$ is given

| | $a_{iso}$ | | $A_i$ | $l_{(gx)i}$ | $l_{(gy)i}$ | $l_{(gz)i}$ | $\phi_v$ | $\phi_g$ |
|---|---|---|---|---|---|---|---|---|
| Cys-549$\beta$1 | 12.9 | *x* | 11.9 | 0.153 | 0.703 | 0.695 | | |
| | | *y* | 10.4 | −0.858 | −0.254 | 0.445 | | |
| | | *z* | 16.3 | 0.490 | −0.665 | 0.564 | 11 | 21 |
| Cys-549$\beta$2 | 11.9 | *x* | 10.8 | 0.099 | 0.496 | 0.863 | | |
| | | *y* | 10.2 | −0.946 | −0.222 | 0.237 | | |
| | | *z* | 14.5 | 0.308 | −0.839 | 0.447 | 31 | 23 |
| Cys-546$\beta$1 | 7.2 | *x* | 6.2 | −0.386 | −0.462 | −0.798 | | |
| | | *y* | 5.6 | −0.528 | −0.599 | 0.601 | | |
| | | *z* | 9.9 | −0.757 | 0.654 | −0.012 | 8 | 6 |
| $H^-$ (bridge) | −8.7 | *x* | −19.8 | −0.061 | 0.978 | 0.198 | 8 | |
| | | *y* | −16.2 | −0.080 | −0.203 | 0.976 | 5 | |
| | | *z* | 9.9 | −0.994 | −0.044 | −0.090 | 9 | |

presence and the binding mode (bridging) of a hydride at the Ni site of catalytic [NiFe]-hydrogenases, which was predicted earlier from comparison of single crystal EPR data and DFT calculations [23].

The complete hyperfine coupling tensors for three distinct protons of the Ni-C state of the hydrogenase from *D. vulgaris* Miyazaki F have been determined from orientation-selected ENDOR spectroscopy. These three couplings are attributed to $\beta$-$CH_2$ protons of the Cys-549 and one $\beta$-$CH_2$ proton of Cys-546, which are consistent with earlier predictions by DFT [25]. Slight deviations between different hydrogenases could be detected and were assigned to small structural differences.

Furthermore, hydrogenase nitrogen couplings have been detected in the HYSCORE spectra of the *D. vulgaris*. These were assigned to the $N_\epsilon$ of His-88, which forms a hydrogen bond to $S_\gamma$(Cys-549). The data analysis and assignment is in full agreement with the detailed study of Buhrke et al. [47] on Ni-C in *R. eutropha* and Chapman et al. [48] on Ni-C in *D. gigas*. Additional nitrogen couplings associated with the [4Fe4S] clusters have been observed. Although the nuclear quadrupole constants could not be determined, these nitrogens are also assigned to His ligands present in the vicinity of the FeS clusters.

Comparison with experimental and theoretical data available for other [NiFe]-hydrogenases reveals a consistent picture in which the $z$ axis of the $3d_{z^2}$ orbital on Ni is directed towards $S_\gamma$(Cys-549) and the free coordination position of Ni. Moreover, the data show that the [NiFe] centers in catalytically-active and regulatory hydrogenases are essentially the same. This suggests that the functional differences of these hydrogenases originate from structural differences further away from the [NiFe] center.

**Acknowledgements** The authors are grateful to Matthias Stein for performing the DFT calculations. Yoshiki Higuchi (Hyogo University, Japan) kindly provided the hydrogenase samples of *D. vulgaris* Miyazaki F. This work has been supported by Deutsche Forschungsgemeinschaft (Sfb 498, TP C2), Fonds der chemischen Industrie (WL), and by the Max Planck Society.

## Appendix

### Choosing signs for the direction cosines from the ENDOR spectra for *D. gigas* hydrogenase

When analyzing orientation-selected ENDOR spectra, information is extracted in the form of principal values of the hyperfine tensor and direction cosines. However, the absolute sign of the direction cosines cannot be determined from analysis of the experimental data.

Müller et al. [26] used their choice of signs for the direction cosines to reconstruct the orientation of the $g$-tensor for Ni-C in *D. gigas* hydrogenase. We propose a different sign choice for the following reasons. (1) By inspecting the field-frequency plot (see Fig. 3, top), protons **a** and **b** are found to be the two most strongly coupled protons and display a similar field-dependence, whereas the curve for proton **c** looks different. This is a strong indication that protons **a** and **b** (or H-A and H-B for *D. gigas* hydrogenase) belong to the same cysteine residue (and likewise protons H-C and H-D in [26]). (2) The assignment of Müller disagrees with the spin-density distribution calculated by two independent groups [16, 24, 25], which indicates that the sulfur of Cys-549 (Cys-533 for *D. gigas*) carries significant spin-density, so the protons of this residue should have the largest hyperfine coupling constants. Calculated proton hyperfine coupling constants from [25] are given in Table 6 for comparison. The calculated spin density distributions show that the principal $z$-axis of the $g$-tensor is directed from nickel towards the vacant coordination position, which is also expected based on ligand field theory. Lastly, the direction cosines of the $x$ axis of proton H-B suggest that the minimum hyperfine coupling of 10.329 MHz (see Table 5) is attained for a molecule oriented such that the effective $g$ value is $[(2.194\times0.283)^2 + 2.146\times0.631)^2 + (2.011\times0.723)^2]^{1/2} = 2.08$. Inspection of the field-frequency plot in [26], however, reveals that proton H-B attains its minimum hyperfine coupling at $g \approx 2.15$. The direction cosines of proton H-B seem to be in disagreement with the corresponding curve in the field-frequency plot of [26]. When the data for *D. gigas* hydrogenase [26] are used with the sign convention and assignment as chosen in the present work, a similar picture is obtained for the Ni-C state in *D. gigas* hydrogenase. Probably, the $g$-tensor for the Ni-C state of *D. gigas* hydrogenase is similar to the one determined by single crystal EPR for *D. vulgaris* hydrogenase [23], which is also compatible with theoretical studies [16, 24, 25].

## References

1. Frey M (1998) Struct Bond 90:97–126
2. Vignais PM, Billoud B, Meyer J (2001) FEMS Microbiol Rev 25:455–501
3. Albracht SPJ (1994) Biochim Biophys Acta 1188:167–204
4. Moura JJG, Moura I, Huynh B-H, Krüger H-J, Teixeira M, DuVarney RC, DerVartanian DV, Xavier AV, Peck HD Jr, LeGall J (1982) Biochem Biophys Res Commun 108:1388–1393
5. Fernandez VM, Hatchikian EC, Patil DS, Cammack R (1986) Biochim Biophys Acta 883:145–154
6. Coremans JMCC, van Garderen CJ, Albracht SPJ (1992) Biochim Biophys Acta 1119:148–156
7. Krasna AI (1978) Method Enzymol 53:296–304
8. van der Zwaan JW, Albracht SPJ, Fontijn RD, Slater EC (1985) FEBS Lett 2:271–277
9. van der Zwaan JW, Albracht SPJ, Fontijn RD, Roelofs YBM (1986) Biochim Biophys Acta 872:208–215
10. Higuchi Y, Yagi T, Yasuoka N (1997) Structure 15:1671–1680
11. Volbeda A, Charon M-H, Hatchikian EC, Frey M, Fontecilla-Camps JC (1995) Nature 373:580–587
12. Volbeda A, Garcin E, Piras C, De Lacey AL, Fernandez VM, Hatchikian EC, Frey M, Fontecilla-Camps JC (1996) J Am Chem Soc 118:12989–12996
13. Rousset M, Montet Y, Guigliarelli B, Forget N, Asso M, Bertrand P, Fontecilla-Camps JC, Hatchikian EC (1998) Proc Natl Acad Sci USA 95:11625–11630

14. Matias PM, Soares CM, Saraiva LM, Coelho R, Morais J, LeGall J, Carrando MA (2001) J Biol Inorg Chem 6:63–81
15. Stein M, van Lenthe E, Baerends EJ, Lubitz W (2001) J Am Chem Soc 123:5839–5840
16. Stadler C, De Lacey AL, Montet Y, Volbeda A, Fontecilla-Camps JC, Conesa JC, Fernandez VM (2002) Inorg Chem 41:4424–4434
17. Carepo M, Tierney DL, Brondino CD, Yang TC, Pamplona A, Telser J, Moura I, Moura JJG, Hoffman BM (2002) J Am Chem Soc 124:281–286
18. Higuchi Y, Ogata H, Miki K, Yasuoka N, Yagi T (1999) Structure 7:549–556
19. Garcin E, Vernede X, Hatchikian EC, Volbeda A, Frey M, Fontecilla-Camps JC (1999) Structure 7:557–566
20. Fan C, Teixeira M, Moura JJG, Moura I, Huynh B-H, LeGall J, Peck HD Jr, Hoffman BM (1991) J Am Chem Soc 113:20–24
21. Whitehead JP, Gurbiel RJ, Bagyinka C, Hoffman BM, Maroney MJ (1993) J Am Chem Soc 115:5629–5635
22. Brecht M, van Gastel M, Buhrke T, Friedrich B, Lubitz W (2003) J Am Chem Soc 125:13075–13083
23. Foerster S, Stein M, Brecht M, Ogata H, Higuchi Y, Lubitz W (2003) J Am Chem Soc 125:83–93
24. Stein M, Lubitz W (2001) Phys Chem Chem Phys 3:2668–2675
25. Stein M, Lubitz W (2001) Phys Chem Chem Phys 3:5115–5120
26. Müller A, Tscherny I, Kappl R, Hatchikian EC, Hüttermann J, Cammack R (2002) J Biol Inorg Chem 7:177–194
27. Yagi T, Kimura K, Daidoji H, Sakai F, Tamura S, Inokuchi H (1976) J Biochem 79:661–671
28. Lide DR (ed)(1992) CRC Handbook of chemistry and physics. Boca Raton, FL
29. Cammack R, Patil DS, Hatchikian EC, Fernandez VM (1987) Biochim Biophys Acta 912:98–109
30. Guigliarelli B, More C, Fournel A, Asso M, Hatchikian EC, Williams R, Cammack R, Bertrand P (1995) Biochemistry 34:4781–4790
31. Zweygart W, Thanner R, Lubitz W (1994) J Magn Reson Ser A 109:172–176
32. Höfer P, Grupp A, Nebenführ H, Mehring M (1986) Chem Phys Lett 132:279–282
33. Shane JJ, Höfer P, Reijerse EJ, de Boer E (1992) J Magn Reson 88:241–256
34. Gemperle C, Aebli G, Schweiger A, Ernst RR (1990) J Magn Reson 88:241–256
35. Fahnenschmidt M (2000) PhD Thesis, TU Berlin, Germany http://edocs.tu-berlin.de
36. Geßner C (1996) PhD Thesis, TU Berlin, Germany
37. van Gastel M, Coremans JWA, Jeuken LJC, Canters GW, Groenen EJJ (1998) J Phys Chem A 102:4462–4470
38. SA Dikanov, Tsvetkov YD (1992) Electron spin echo envelope modulation (ESEEM) spectroscopy. CRC, Boca Raton, FL
39. Pöppl A, Kevan L (1996) J Phys Chem 100:3387–3394
40. Flanagan HL, Singel DJ (1987) J Chem Phys 87:5606–5616
41. Sorgenfrei O, Klein A, Albracht SPJ (1993) FEBS Lett 332:291–297
42. van der Zwaan JW, Coremans JMCC, Bouwens ECM, Albracht SPJ (1990) Biochim Biophys Acta 1041:101–110
43. Dole F, Medina M, More C, Cammack R, Bertrand P, Guigliarelli B (1996) Biochemistry 35:16399–16406
44. De Lacey AL, Hatchikian EC, Volbeda A, Frey M, Fontecilla-Camps JC, Fernandez VM (1997) J Am Chem Soc 119:7181–7189
45. Coremans JMCC, van der Zwaan JW, Albracht SPJ (1989) Biochim Biophys Acta 997:256–267
46. Jiang F, McCracken J, Peisach J (1990) J Am Chem Soc 112:9035–9044
47. Buhrke T, Brecht M, Lubitz W, Friedrich B (2002) J Biol Inorg Chem 7:897–908
48. Chapman A, Cammack R, Hatchikian EC, McCracken J, Peisach J (1988) FEBS Lett 242:134–138